

This is an Open Access document downloaded from ORCA, Cardiff University's institutional repository:<https://orca.cardiff.ac.uk/id/eprint/129514/>

This is the author's version of a work that was submitted to / accepted for publication.

Citation for final published version:

Hong, John, Lee, Young-Woo, Ahn, Docheon, Pak, Sangyeon, Lee, Juwon, Jang, A-Rang, Lee, Sanghyo, Hou, Bo, Cho, Yuljae, Morris, Stephen M., Shin, Hyeon Suk, Cha, SeungNam, Sohn, Jung Inn and Kim, Jong Min 2017. Highly stable 3D porous heterostructures with hierarchically-coordinated octahedral transition metals for enhanced performance supercapacitors. *Nano Energy* 39, pp. 337-345.  
10.1016/j.nanoen.2017.07.010

Publishers page: <http://dx.doi.org/10.1016/j.nanoen.2017.07.010>

Please note:

Changes made as a result of publishing processes such as copy-editing, formatting and page numbers may not be reflected in this version. For the definitive version of this publication, please refer to the published source. You are advised to consult the publisher's version if you wish to cite this paper.

This version is being made available in accordance with publisher policies. See <http://orca.cf.ac.uk/policies.html> for usage policies. Copyright and moral rights for publications made available in ORCA are retained by the copyright holders.



1  
2  
3  
4  
5  
6  
7  
8  
9  
10  
11  
12  
13  
14  
15  
16  
17  
18  
19  
20  
21  
22  
23  
24  
25  
26  
27  
28  
29  
30  
31  
32  
33  
34  
35  
36  
37  
38  
39  
40  
41  
42  
43  
44  
45

# Bimodal-Hierarchically Assembled 3-Dimensional ZnCo<sub>2</sub>O<sub>4</sub>/NiMoO<sub>4</sub> Heterostructures Enabling Efficient and Robust Energy Storage Performance

*John Hong,<sup>†,‡</sup> Young-Woo Lee,<sup>†,‡</sup> Docheon Ahn,<sup>⊥</sup> Sangyeon Pak,<sup>†</sup> Juwon Lee,<sup>†</sup> A-Rang Jang,<sup>†,||</sup>*

*Sanghyo Lee,<sup>†</sup> Bo Hou,<sup>†</sup> Yuljae Cho,<sup>†</sup> Stephen M. Morris,<sup>†</sup> Hyeon Suk Shin,<sup>||,\*</sup> SeungNam Cha,<sup>†</sup>*

*Jung Inn Sohn,<sup>†,\*</sup> and Jong Min Kim<sup>¶</sup>*

<sup>†</sup> Department of Engineering Science, University of Oxford, Oxford OX1 3PJ, United Kingdom.

<sup>⊥</sup> Beamline Department, Pohang Accelerator Laboratory, Pohang 37673, Republic of Korea.

<sup>||</sup> Department of Chemistry, Ulsan National Institute of Science and Technology (UNIST), Ulsan 689-798, Republic of Korea.

<sup>¶</sup> Electrical Engineering Division, Department of Engineering, University of Cambridge, Cambridge CB3 0FA, United Kingdom.

**KEYWORDS.** hierarchical assembly, heterostructures, porous network structure, ternary transition metal oxides, supercapacitors

46  
47  
48  
49  
50  
51  
52  
53  
54  
55  
56  
57  
58  
59  
60

1  
2  
3 **ABSTRACT.** Designing and tailoring the assembly of complex ternary transition metal oxide  
4  
5 (TTMO) structures are a key step in the pursuit of high performance pseudo-capacitive materials  
6  
7 for the development of next-generation energy storage devices. Here, we present uniquely  
8  
9 assembled 3D heterostructures with hierarchically bimodal morphological features, consisting of  
10  
11 a rigidly interconnected primary nanoporous framework of ZnCo<sub>2</sub>O<sub>4</sub>/NiMoO<sub>4</sub> core-shell  
12  
13 structures and a secondary protruding structure of NiMoO<sub>4</sub> layered nanosheets. By benefiting  
14  
15 from the combination of the two TTMOs, each with distinct physical characteristics, the  
16  
17 assembled 3D ZnCo<sub>2</sub>O<sub>4</sub>/NiMoO<sub>4</sub> heterostructures exhibit excellent pseudo-capacitive  
18  
19 performance with high capacitances of 6.07 F cm<sup>-2</sup> and 1480.48 F g<sup>-1</sup> at 2 mA cm<sup>-2</sup> as well as an  
20  
21 excellent cycling stability of 90.6% over 15000 cycles. Moreover, an asymmetric supercapacitor  
22  
23 device can deliver a high energy density of 48.6 Wh kg<sup>-1</sup>. The superior pseudo-capacitive energy  
24  
25 storage characteristics are strongly attributed to the interconnected 3D nanoporous network  
26  
27 architecture of the TTMOs along with the secondary layered nanosheets that provide 1) an  
28  
29 enlarged surface area, 2) facile and multi-access ion paths, and 3) favorable structural stability.  
30  
31 Combined, these results highlight the importance of novel nanostructure design in maximizing  
32  
33 the pseudo-capacitive performance and provides a viable way to develop new electrode  
34  
35 materials.  
36  
37  
38  
39  
40  
41  
42  
43  
44  
45  
46  
47  
48  
49  
50  
51  
52  
53  
54  
55  
56  
57  
58  
59  
60

## 1. Introduction.

Pseudo-capacitors, which are an emerging class of electrochemical energy storage system, have been intensively studied over the past few decades in an attempt to address the rapidly increasing global energy requirements whilst also considering the corresponding impact on the economy and the environment.<sup>1-4</sup> The significant importance of pseudo-capacitors as future energy storage devices stems from the fact that, theoretically, they are capable of providing a power delivery and stable cyclability that is superior to that exhibited by Li-ion batteries. In addition, they are also capable of storing a higher energy density than that of electrical double layer capacitors.<sup>5-7</sup> Recent studies have recognized that even though the performance of pseudo-capacitors is essentially determined by the intrinsic physical and chemical properties of the electrode materials, the structural design of the electrode materials can also greatly influence the resulting pseudo-capacitive charge storage behavior as well as the electrochemical kinetics.<sup>8,9</sup> As a result, a tremendous amount of effort has been directed towards the development of carefully structured electrode materials with a controllable size, morphology, stoichiometry, and hierarchical architecture. The aim of this work has been to enlarge the electrochemically active regions to enable faster electrochemical kinetics, which in turn can lead to both higher energy and higher power densities.<sup>10-12</sup>

To date, it has been widely proposed and generally accepted that structural engineering of the electrode materials, through the miniaturization of the size as well as the construction of a porous-structure, is an effective and viable strategy towards steadily improving many transition metal oxides for pseudo-capacitive applications.<sup>13,14</sup> Despite these notable technological advances, it still remains a challenge to tailor complex ternary transition metal oxides (TTMOs), which has the advantage of combining two different mono-component metal oxides into

1  
2  
3 desirable nanostructured architectures with a maximized surface area, facile and short ion  
4  
5 diffusion paths, and a high structural integrity during the charge/discharge process.  
6  
7

8 Inspired by a basic spinel structural model with 3 dimensional (3D) open channels,<sup>15</sup> in this  
9  
10 study, we propose hierarchically assembled 3D heterostructures that comprise a rigidly  
11  
12 interconnected nanoporous core-shell network and a secondary protruding nanostructure as  
13  
14 illustrated in Figure 1a. Such a proposed electrode design can be expected to enable  
15  
16 enhancement of the electrochemical features of the properly selected TTMO electrode beyond  
17  
18 the aforementioned requirements for the next generation energy storage devices. Among the  
19  
20 various TTMO candidates,  $\text{ZnCo}_2\text{O}_4$  is considered as an ideal backbone material (core) for the  
21  
22 robust, porous, and conductive 3D architecture due to the combination of its excellent intrinsic  
23  
24 electrical conductivity and its unique cubic spinel crystal structure, which is highly stable and  
25  
26 consists of large internal voids as well as 3D internal channels for rapid and multiple access of  
27  
28 the ions.<sup>16,17</sup> On the other hand,  $\text{NiMoO}_4$  is considered to be a potential pseudo-capacitive  
29  
30 material for the shell and secondary protruding structure because the excellent redox behavior of  
31  
32 the Ni atoms and the good electrical conductivity of the Mo atoms can contribute collectively to  
33  
34 yield a high pseudo-capacitive performance.<sup>18,19</sup> Moreover, the open space between the  
35  
36 octahedral Ni sites and the tetrahedral Mo sites along with the nanoscale architecture can be  
37  
38 particularly beneficial in terms of enhancing the pseudo-capacitive kinetics.  
39  
40  
41  
42  
43  
44

45 Herein, we report a novel and unique bottom-up synthetic assembly of 3D  $\text{ZnCo}_2\text{O}_4/\text{NiMoO}_4$   
46  
47 heterostructures with sponge-like primary nanoporous plates along with a secondary protruding  
48  
49 layered nanosheet arrays. The electrodes that are directly integrated onto the 3D microporous  
50  
51 current collector provide a unique configuration that consists of a porous and layered network  
52  
53 resulting in an enlarged active surface area and multi-access channel. This structure also exhibits  
54  
55  
56  
57  
58  
59  
60

1  
2  
3 a superior structural integrity that can accommodate any mechanical stress that is induced when  
4  
5 cycling through the charge/discharge process, ensuring a favorable electrochemical performance.  
6  
7  
8

## 9 10 **2. Results and Discussion**

11  
12 The synthetic process for the hierarchically assembled 3D ZnCo<sub>2</sub>O<sub>4</sub>/NiMoO<sub>4</sub> electrode  
13  
14 structure is shown in Figure 1b. The ZnCo<sub>2</sub>O<sub>4</sub>/NiMoO<sub>4</sub> heterostructures were fabricated using  
15  
16 stepwise bottom-up assembly synthesis procedure. Firstly, the nanoporous plate-like structure of  
17  
18 ZnCo<sub>2</sub>O<sub>4</sub> was prepared on a 3D microporous current collector (left of Figure 1b) so as to serve as  
19  
20 the rigid backbone structure, which is expected to combine properties of high conductivity,  
21  
22 structural stability, and a desirable porous structure (middle of Figure 1b). Then, the resultant  
23  
24 nanoporous ZnCo<sub>2</sub>O<sub>4</sub> plates were uniformly coated by the active nanoscale NiMoO<sub>4</sub> shell layers,  
25  
26 along with the formation of the layered NiMoO<sub>4</sub> nanosheets on the surface of the interconnected  
27  
28 core-shell network using a subsequent bottom-up synthesis method (right of Figure 1b). As a  
29  
30 result, electrodes with two distinct primary and secondary nanostructures were successfully  
31  
32 prepared, enabling rich, rapid, and stable Faradaic redox reactions for pseudo-capacitors.  
33  
34  
35

36  
37 The hierarchically assembled 3D ZnCo<sub>2</sub>O<sub>4</sub>/NiMoO<sub>4</sub> heterostructures were assessed by  
38  
39 scanning electron microscopy (SEM), transmission electron microscopy (TEM), and high-angle  
40  
41 annular dark-field scanning TEM (HAADF-STEM) measurements. It can be seen that very thin  
42  
43 nanostructured ZnCo<sub>2</sub>O<sub>4</sub> plates with uniform and smooth surface morphology are dispersed  
44  
45 across the entire 3D microporous current collector (Figure 2a and S1a-b). TEM studies reveal  
46  
47 that the plates are composed of the rigidly interconnected nanoscale grains and pores with a size  
48  
49 of 10–20 nm, as shown in Figure 2b and S1c. Moreover, Figure 2c presents the HAADF-STEM  
50  
51 image of ZnCo<sub>2</sub>O<sub>4</sub>, further demonstrating the existence of the highly-entangled grains (white  
52  
53  
54  
55  
56  
57  
58  
59  
60

1  
2  
3 space) and pore channels (black space). The elemental distribution of the  $\text{ZnCo}_2\text{O}_4$  plates is also  
4  
5 clearly identified by the energy dispersive X-ray spectroscopy (EDX) mapping analysis (Figure  
6  
7 2d), confirming that the Zn, Co, and O elements are uniformly dispersed on the nanoporous  
8  
9 plates.  
10

11  
12 After a hierarchical bottom-up assembly process to develop the 3D  $\text{ZnCo}_2\text{O}_4/\text{NiMoO}_4$   
13  
14 heterostructures, there is an obvious change in the surface morphology of the electrodes with the  
15  
16 addition of the secondary nanosheet arrays that protrude from the backbone plate structure, as  
17  
18 shown in Figure 2e and S2a-b. Notably, STEM and HAADF-STEM images show  
19  
20 morphologically distinct regions, including a primary plate region with an interconnected porous  
21  
22 network (the center region in Figure 2f-g and S2c-e, see more detailed information in SI) and the  
23  
24 secondary nanosheet region (the edge region in Figure 2f-g). Furthermore, the EDX mapping  
25  
26 images taken from the area in the HAADF-STEM image of Figure 2g and inset of Figure S2e  
27  
28 show that all the elements (Zn, Co, Ni, and Mo) are uniformly distributed along the hierarchical  
29  
30 nanostructures (Figure 2h and S2f). Therefore, these results indicate the formation of  
31  
32  $\text{ZnCo}_2\text{O}_4/\text{NiMoO}_4$  heterostructures with additional secondary nanostructures.  
33  
34  
35  
36  
37

38 To further investigate the detailed structural features of the hierarchically assembled 3D  
39  
40  $\text{ZnCo}_2\text{O}_4/\text{NiMoO}_4$  heterostructures, a high-resolution HAADF-STEM image was recorded from  
41  
42 the center region of the sample as shown in Figure 3a. The corresponding EDX mapping images  
43  
44 show the clear coexistence of all four metal elements on the whole area of the sample (Figure  
45  
46 3b). Interestingly, the EDX signals of the Ni and Mo atom were detected with relatively high  
47  
48 intensity on the white dotted area. These findings are believed to be strongly associated with the  
49  
50 formation of the secondary  $\text{NiMoO}_4$  nanosheets on the surface of the  $\text{ZnCo}_2\text{O}_4$  plates. Moreover,  
51  
52 Figure 3c-d show atomic scale structural characterization of the  $\text{ZnCo}_2\text{O}_4/\text{NiMoO}_4$   
53  
54  
55  
56  
57  
58  
59  
60

1  
2  
3 heterostructures further investigated by the high-resolution TEM images and the corresponding  
4 fast Fourier transform diffraction (FFT) patterns from the region outlined by a yellow dotted  
5 rectangle as shown in Figure 3a. These TEM and FFT results clearly reveal two distinct regions  
6  
7  
8 in the  $\text{ZnCo}_2\text{O}_4/\text{NiMoO}_4$  heterostructures: (1) the region 1 is found to be a primary  
9  
10 heterostructure region consisting of the active  $\text{NiMoO}_4$  shell and rigid  $\text{ZnCo}_2\text{O}_4$  core structures,  
11  
12 which are determined by three different adjacent lattice spacings of about 0.238, 0.145, and  
13  
14 0.210 nm, which correspond to a (311) plane of spinel  $\text{ZnCo}_2\text{O}_4$ , and (600) and (330) planes of  
15  
16 monoclinic  $\text{NiMoO}_4$ , respectively;<sup>20, 21</sup> (2) the region 2 is identified as the secondary structure  
17  
18 region associated with the layered  $\text{NiMoO}_4$  nanosheet structure from the observation of lattice  
19  
20 fringes with only 0.215 nm spacing, indicating the (400) planes of monoclinic  $\text{NiMoO}_4$ .<sup>[21]</sup> In  
21  
22 addition, the cross sectional HAADF-STEM (Figure 3e-f and S3a) and EDX mapping (Figure  
23  
24 S3b) images of the  $\text{ZnCo}_2\text{O}_4/\text{NiMoO}_4$  heterostructures prepared using a focused ion beam also  
25  
26 clearly verify the hierarchical formation of secondary protruding layered nanosheets on the  
27  
28 primary nanoporous plates.

29  
30  
31  
32  
33  
34  
35  
36  
37  
38  
39  
40  
41  
42  
43  
44  
45  
46  
47  
48  
49  
50  
51  
52  
53  
54  
55  
56  
57  
58  
59  
60

Synchrotron X-ray diffraction (XRD) and X-ray photoelectron spectroscopy (XPS) analysis was also performed to further verify the crystal and chemical structures of the hierarchically assembled 3D  $\text{ZnCo}_2\text{O}_4/\text{NiMoO}_4$  heterostructures. As shown in Figure S4 (see more detailed information in SI), all the reflections in the XRD patterns are unambiguously assigned to spinel  $\text{ZnCo}_2\text{O}_4$  (JCPDS 23-1390) and monoclinic  $\text{NiMoO}_4$  (JCPDS 86-0361).<sup>22,23</sup> Moreover, Figure 3g shows high-resolution XPS spectra of the Zn 2p, Co 2p, Ni 2p and Mo 3d peak regions with the fitted peak components, clearly revealing the presence of the corresponding metallic elements. This is in good agreement with the EDX results as shown in Figure 2h and 3b. The peak fitting analysis of all the XPS spectra suggests that there exist the compositions of  $\text{Zn}^{2+}$  and  $\text{Co}^{3+}$  in the



1  
2  
3 ZnCo<sub>2</sub>O<sub>4</sub> structure, and the Ni and Mo exist as Ni<sup>2+</sup> and Mo<sup>6+</sup> states, respectively, in the NiMoO<sub>4</sub>  
4  
5 structure.<sup>24,25</sup> Thus, a comparison of the SEM, TEM, EDX, XRD, and XPS results provides  
6  
7 direct evidence that the 3D assembled ZnCo<sub>2</sub>O<sub>4</sub>/NiMoO<sub>4</sub> heterostructures consist of the primary  
8  
9 ZnCo<sub>2</sub>O<sub>4</sub>/NiMoO<sub>4</sub> plates and the secondary layered NiMoO<sub>4</sub> nanosheet arrays.

10  
11  
12 On the basis of the obtained heterostructures and chemical composition information, we have  
13  
14 evaluated the pseudo-capacitive characteristics of the hierarchically assembled 3D  
15  
16 ZnCo<sub>2</sub>O<sub>4</sub>/NiMoO<sub>4</sub> heterostructures. Figure 4 depicts the overall electrochemical performance of  
17  
18 the bare ZnCo<sub>2</sub>O<sub>4</sub> electrode without any additional NiMoO<sub>4</sub> layer (denoted as single-TTMO) and  
19  
20 the ZnCo<sub>2</sub>O<sub>4</sub>/NiMoO<sub>4</sub> heterostructured electrode with hierarchically bimodal geometrical  
21  
22 structures (denoted as bimodal-TTMO). As shown in Figure 4a, a cyclic voltammetry (CV)  
23  
24 curve of the bimodal-TTMO exhibits the typical Faradaic redox behavior with a potential  
25  
26 window ranging from 0.0 to 0.6 V at a scan rate of 5 mV s<sup>-1</sup>. The integrated CV area for the  
27  
28 bimodal-TTMO sample is much larger than that of the single-TTMO. This indicates that the  
29  
30 bimodal-TTMO possesses a superior electrochemical capacitance due to the unique hierarchical  
31  
32 core-shell nanostructures with a relatively high surface area, which is consistent with the  
33  
34 Brunauer-Emmett-Teller (BET) surface area measurement results (Figure S5). Moreover, all CV  
35  
36 curves have similar shapes within scan rates of 5–50 mV s<sup>-1</sup>, indicating reversible Faradaic  
37  
38 reaction behavior (Figure S6a). Further, we plotted the cathodic and anodic current densities as a  
39  
40 function of the scan rates from the CV curves of the bimodal-TTMO and have clearly observed a  
41  
42 linear relationship with the oxidation reaction ( $R^2 = 0.99959$ ) and reduction reaction ( $R^2 =$   
43  
44  $0.99886$ ) values (Figure S6b). These high values of  $R^2$ , close to 1, also imply that our bimodal-  
45  
46 TTMO electrode exhibits good reversible redox reaction behavior.<sup>26</sup>  
47  
48  
49  
50  
51  
52  
53  
54  
55  
56  
57  
58  
59  
60

1  
2  
3 Figure 4b presents galvanostatic charge/discharge (GCD) curves of the bimodal-TTMO at  
4 different current densities. Similar to the CV results, the bimodal-TTMO electrode shows typical  
5 charge/discharge curves with superior Faradaic redox reaction performance compared to the  
6 single-TTMO electrode as shown in Figure S7a. As expected, the area and mass capacitance of  
7 the bimodal-TTMO are significantly enhanced to reach  $6.07 \text{ F cm}^{-2}$  and  $1480.48 \text{ F g}^{-1}$ ,  
8 respectively, at a current density of  $2 \text{ mA cm}^{-2}$  (Figure 4c), which are 4 times more than that of  
9 the specific capacitance of the single-TTMO (Figure S7b). Moreover, even at a high current  
10 density of  $50 \text{ mA cm}^{-2}$ , the bimodal-TTMO electrode can achieve a capacitance of up to  $959.04$   
11  $\text{F g}^{-1}$  even at a high current density of  $50 \text{ mA cm}^{-2}$ .  
12  
13  
14  
15  
16  
17  
18  
19  
20  
21  
22  
23

24 In addition to demonstrating the substantive electrochemical capacitive performance, we also  
25 conducted electrochemical cycling tests to evaluate the capacitance retention capability and  
26 structural stability of the electrode. Obviously, it can be seen that the electrode remarkably  
27 retains more than 96.8% of its initial capacitance after 3000 cycles at  $50 \text{ mV s}^{-1}$  (Figure 4d),  
28 which shows a superior capacitance retention compared to other reported ternary transition metal  
29 oxide electrodes, as summarized in Table S1. It should be noted that under harsh conditions, the  
30 bimodal-TTMO exhibits excellent electrochemical cyclability with a capacitance retention of  
31 90.6% after 15000 cycles at a high scan rate of  $100 \text{ mV s}^{-1}$  (Figure 4e). Inset images of Figure 4e  
32 present Nyquist plots (left) and Bode phase plots (right) of the bimodal-TTMO electrode  
33 obtained using electrochemical impedance spectroscopy (EIS) measurements to analyze the  
34 electrochemical kinetics and stability of the electrode before and after the charge/discharge  
35 cycling test. It can be clearly seen that in the Nyquist plots, even after 15000 cycles, semicircles  
36 at the high frequency region and straight lines at the low frequency region, which indicate the  
37 charge transfer resistance ( $R_{ct}$ ) and the Warburg impedance (W) associated with ion diffusion  
38  
39  
40  
41  
42  
43  
44  
45  
46  
47  
48  
49  
50  
51  
52  
53  
54  
55  
56  
57  
58  
59  
60

1  
2  
3 processes, respectively, almost remain unchanged. Moreover, it is also observed that in the Bode  
4  
5 plot, the phase angle at low frequency can be maintained at about  $\sim -77^\circ$  (the degree for ideal  
6  
7 capacitor behavior is close to  $-90^\circ$ )<sup>27</sup> over the long-term cycling test. These EIS results indicate  
8  
9 that the bimodal-TTMO electrode has superior electrochemical kinetics and stability and hence  
10  
11 retains its excellent capacitive behavior during the charge/discharge processes. Additionally, we  
12  
13  
14 further analyzed morphological changes of the electrode to investigate the structural stability  
15  
16 after long-term cycling testing using SEM examinations as shown in Figure S8. It is revealed that  
17  
18 the morphology and the structure of the hierarchical 3D ZnCo<sub>2</sub>O<sub>4</sub>/NiMoO<sub>4</sub> heterostructured  
19  
20  
21 electrode remain intact after 15000 cycling tests, demonstrating its structural robustness.

22  
23  
24 From the point of view of electrode design and material properties, our uniquely designed  
25  
26 electrode has multiple distinct advantages that enable superior electrochemical performance, as  
27  
28 illustrated in Figure 4f. The first is the hierarchically assembled 3D heterostructures with open  
29  
30 interconnected porous channels, providing enhanced surface area and multi-access diffusion  
31  
32 pathways for facile and rapid ion transport. The second advantage is the formation of the  
33  
34 secondary protruding NiMoO<sub>4</sub> nanosheets on the surface of the primary nanoplates, which  
35  
36  
37 provide an additional contribution to the improvement of the specific capacitance and  
38  
39 electrochemical kinetics because of the high pseudo-capacitive activity combined with the  
40  
41 unique layered, open structure that facilitates favorable ion diffusion and adsorption. An  
42  
43  
44 additional advantage of our electrode design is that the direct integration of the ZnCo<sub>2</sub>O<sub>4</sub>  
45  
46 backbone structure, which has high electric conductivity and good structural stability, onto the  
47  
48 3D microporous current collector framework ensures fast electron transport and good structural  
49  
50 integrity (Figure S6c, see more detailed information in SI), but also stimulates more surface area  
51  
52  
53 of the NiMoO<sub>4</sub> to become electrochemically active.  
54  
55  
56  
57  
58  
59  
60

1  
2  
3 To further evaluate the bimodal-TTMO electrode for practical applications, we fabricated an  
4 asymmetric supercapacitor (ASC) coin cell with activated carbon (AC) as the anode and the  
5 bimodal-TTMO as the cathode. From CV curves of the AC and bimodal-TTMO electrodes  
6 (Figure S9a), we have calculated the mass of the AC anode to fulfill the charge balance with the  
7 bimodal-TTMO cathode and estimated that the AC//bimodal-TTMO ASC can be operated in a  
8 wide potential range from 0 to 1.6 V.<sup>28</sup> Figure S9b presents the CV curves collected at different  
9 operating voltage windows at a scan rate of 50 mV s<sup>-1</sup>, showing capacitance contribution from  
10 both the AC anode and the bimodal-TTMO cathode. The inset of Figure S9c depicts typical  
11 GCD curves of the ASC at current densities from 20 to 2 mA cm<sup>-2</sup> within a potential range of 0  
12 to 1.6 V. Accordingly, the maximum specific capacitance of the ASC reaches 136.6 F g<sup>-1</sup> at a  
13 current density of 2 mA cm<sup>-2</sup> (Figure S9c).  
14

15  
16  
17  
18  
19  
20  
21  
22  
23  
24  
25  
26  
27  
28 On the basis of the GCD curves, the specific energy density and power density of the ASC  
29 were calculated. Figure 5a presents the Ragone plot of the AC//bimodal-TTMOs ASC for the  
30 purposes of comparison with other devices reported recently. The ASC device exhibits a high  
31 energy density of 48.6 Wh kg<sup>-1</sup> and also reaches a reasonable power density ranging from 112.7  
32 to 2820 W kg<sup>-1</sup>. The practical electrochemical performance of our ASC are much higher than  
33 those of other reported devices and commercial energy storage devices.<sup>29-37</sup> Moreover, the ASC  
34 exhibits excellent cycle life with a capacitance retention of 94.0% after 3000 cycles at a scan rate  
35 of 50 mV s<sup>-1</sup> (Figure 5b). These findings suggest that our ASC device can be used as a promising  
36 energy storage system with reliable long-term operation durability. Additionally, we have  
37 demonstrated that our optimized three ASC coin cells connected in series can successfully power  
38 up to 29 red light-emitting diodes (LEDs) which were assembled in parallel (Inset of Figure 5b  
39 and Figure S10).  
40  
41  
42  
43  
44  
45  
46  
47  
48  
49  
50  
51  
52  
53  
54  
55  
56  
57  
58  
59  
60

### 3. Conclusions

In summary, we have reported hierarchically assembled 3D heterostructures of two different TTMOs to emphasize the importance of designing nanoarchitectures that optimize the intrinsic electrochemical properties and provide a morphology that exhibits a high structural integrity. Such a novel electrode design confirms the significance of the hierarchical nanostructures and the realization of the bimodal-TTMOs as a pseudo-capacitive cathode electrode. Importantly, the synergistic effects of bimodal-TTMOs within their unique interconnected nanoporous network structure, combining with an enlarged contact area, plausible electrochemical kinetics in ion/charge transport and great mechanical stability have been reported, exhibiting a high specific capacitance and a superior long-term cyclability over 15000 charge/discharge cycles. Moreover, the asymmetric coin cell supercapacitor can deliver a high energy density of  $48.6 \text{ Wh kg}^{-1}$  and a high power density of  $2820 \text{ W kg}^{-1}$ . Further, it is expected that our approach for rationally designing and tailoring the hierarchical bimodal-TTMO electrode has great potential for energy storage technologies and also contributes to many other application areas dealing with electrochemical processes and ion/charge transport kinetics within nanoporous network structures.

### 4. Experimental Section

**Synthesis of hierarchically nanostructured  $\text{ZnCo}_2\text{O}_4/\text{NiMoO}_4$  heterostructures.** All the chemicals were of analytical grade and directly used after purchase without further purification steps. Hierarchically assembled 3D  $\text{ZnCo}_2\text{O}_4/\text{NiMoO}_4$  heterostructures on a Ni foam were synthesized by a two-step hydrothermal synthetic process. Prior to the hydrothermal synthesis,

1  
2  
3 the conductive Ni foam was cleaned by sonification using 1.0 M HCl, ethanol, and deionized  
4  
5  
6 water. For the synthesis of the ZnCo<sub>2</sub>O<sub>4</sub> core backbone material, 1.0 mmol of Zn(NO<sub>3</sub>)<sub>2</sub>·6H<sub>2</sub>O,  
7  
8 2.0 mmol of Co(NO<sub>3</sub>)<sub>2</sub>·6H<sub>2</sub>O and 5.0 mmol of urea were dissolved in deionized water to form a  
9  
10 clear red solution. The red solution and the cleaned Ni foam were then transferred into a Teflon-  
11  
12 lined stainless steel autoclave and kept at 130 °C for 5 h. After cooling down, the Ni foam  
13  
14  
15 sample was rinsed several times to remove impurities and dried at 60 °C for 12 h. In order to  
16  
17 obtain the crystallized nanoporous ZnCo<sub>2</sub>O<sub>4</sub>, the Ni foam sample was annealed at 350 °C for 2 h  
18  
19 with a heating rate of 1 °C min<sup>-1</sup> under Ar environment. Then, to obtain hierarchically assembled  
20  
21  
22 3D ZnCo<sub>2</sub>O<sub>4</sub>/NiMoO<sub>4</sub> heterostructures, precursors for NiMoO<sub>4</sub> were prepared. For this, 1.0  
23  
24 mmol of Ni(NO<sub>3</sub>)<sub>2</sub>·6H<sub>2</sub>O and 1.0 mmol of Na<sub>2</sub>MoO<sub>4</sub> were dissolved in a mixture solution  
25  
26 (deionized water and ethanol) to form a clear green solution. The green solution and the annealed  
27  
28  
29 Ni foam sample with a nanoporous ZnCo<sub>2</sub>O<sub>4</sub> core were transferred into the Teflon-lined stainless  
30  
31 steel autoclave and kept at 140 °C for 4 h. Finally, after the same cooling and rinsing steps, the  
32  
33 Ni foam sample was annealed at 350 °C for 2 h under the same heating rate and environmental  
34  
35  
36 conditions.

37  
38  
39  
40 **Electrochemical Characterization.** The electrochemical performance of the obtained  
41  
42 electrodes was tested in a three-electrode configuration consisting of the sample as the working  
43  
44  
45 electrode, a Pt mesh as the counter electrode, and a saturated Ag/AgCl electrode as the reference  
46  
47 electrode. CV (within the range of 0.0–0.6 V), GCD (within the range of 0.0–0.5 V), and EIS (in  
48  
49 the range of 10<sup>-2</sup> to 10<sup>5</sup> Hz) examinations were conducted using a potentiostat analysis system  
50  
51 (PGSTAT302N, Metrohm Autolab). The specific areal and mass capacitance can be calculated  
52  
53  
54 according to the following Equation 1:

$$C_A = \frac{I_d * t}{\Delta V * A}, C_m = \frac{I_d * t}{\Delta V * m} \quad (1)$$

where  $C_A$  is the specific areal capacitance,  $C_m$  is the specific mass capacitance,  $I_d$  is the discharge current,  $t$  is the discharge time,  $\Delta V$  is the operating potential during the discharge process,  $A$  is the active area of the sample, and  $m$  is the mass of the active material. The loading mass of the active materials is  $2.1 \text{ mg cm}^{-2}$  and  $4.1 \text{ mg cm}^{-2}$  for the  $\text{ZnCo}_2\text{O}_4$  and the  $\text{ZnCo}_2\text{O}_4/\text{NiMoO}_4$  samples, respectively. The active carbon (AC)// $\text{ZnCo}_2\text{O}_4/\text{NiMoO}_4$  asymmetric supercapacitor (ASC) was prepared to test the full cell performance by fabricating a 2032-coin cell. The ASC was fabricated by using the AC as the anode material, the  $\text{ZnCo}_2\text{O}_4/\text{NiMoO}_4$  heterostructure sample as the cathode material, a cellulose paper as the separator and 6.0 M KOH as the electrolyte solution. The charge balance and the loading mass of the AC electrode were optimized according to the following Equation 2:

$$Q_+ = Q_- \Rightarrow \frac{m_+}{m_-} = \frac{C_- * \Delta V_-}{C_+ * \Delta V_+} \quad (2)$$

where  $C_+$  and  $C_-$  are the specific capacitance of the cathode and anode electrodes, respectively, and  $\Delta V_+$  and  $\Delta V_-$  are the operating potential windows of the cathode and anode electrodes, respectively. The AC anode was constructed by using the active carbon as the active material, poly(vinylidene difluoride) as the binder, and Ketjen black as the conductive material. This solution was coated onto a compressed Ni foam as the current collector. The energy density and power density of the ASC can be calculated according to the following Equation 3:

$$E(\text{energy}) = \frac{1}{2} C_m \Delta V^2 \text{ and } P(\text{power}) = \frac{E}{t} \quad (3)$$

where  $C_m$  is the specific overall capacitance,  $E$  is the calculated energy density,  $\Delta V$  is the overall

operating potential window, and  $t$  is the discharge time.



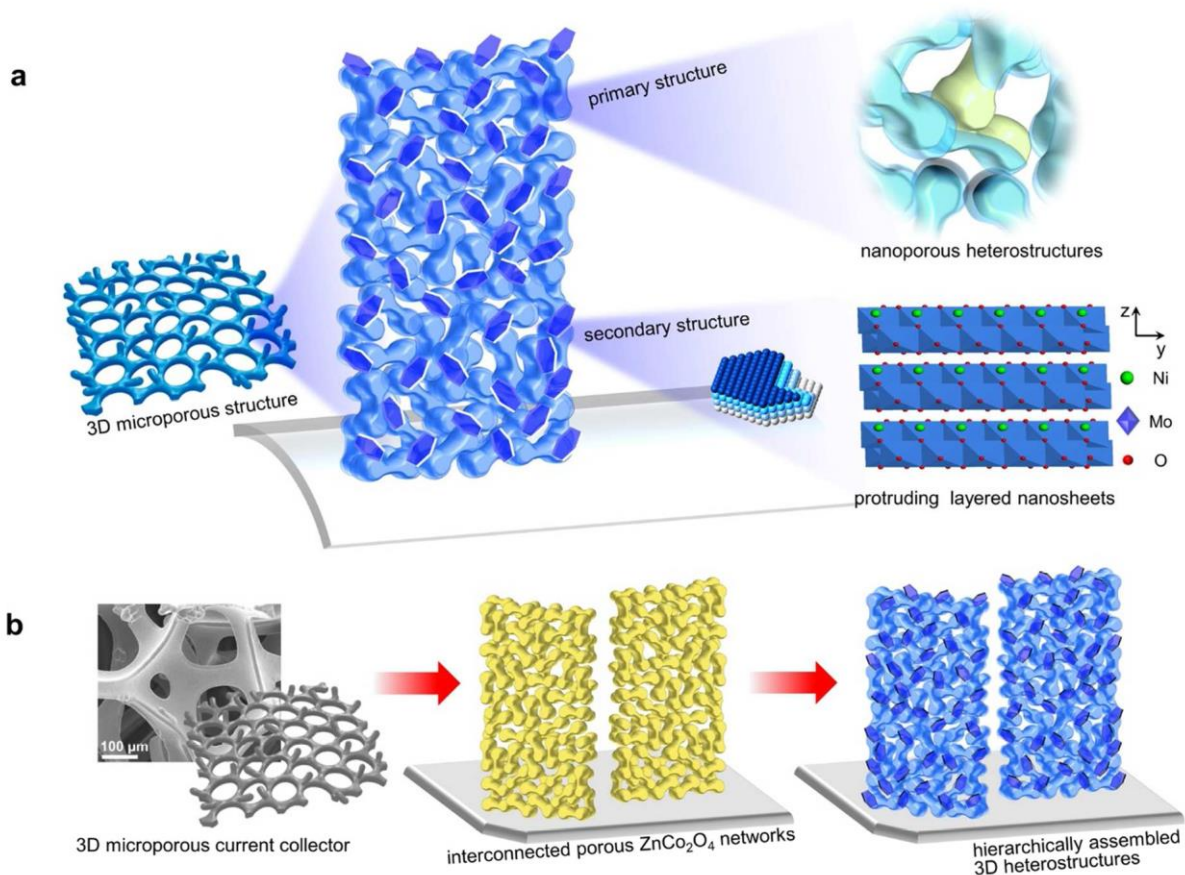


Figure 1. Illustrations of (a) the overall hierarchically assembled 3D ZnCo<sub>2</sub>O<sub>4</sub>/NiMoO<sub>4</sub> heterostructures and (b) the fabrication steps for 3D ZnCo<sub>2</sub>O<sub>4</sub>/NiMoO<sub>4</sub> heterostructures directly integrated on the 3D microporous conductive current collector through hierarchical bottom-up synthesis assembly.

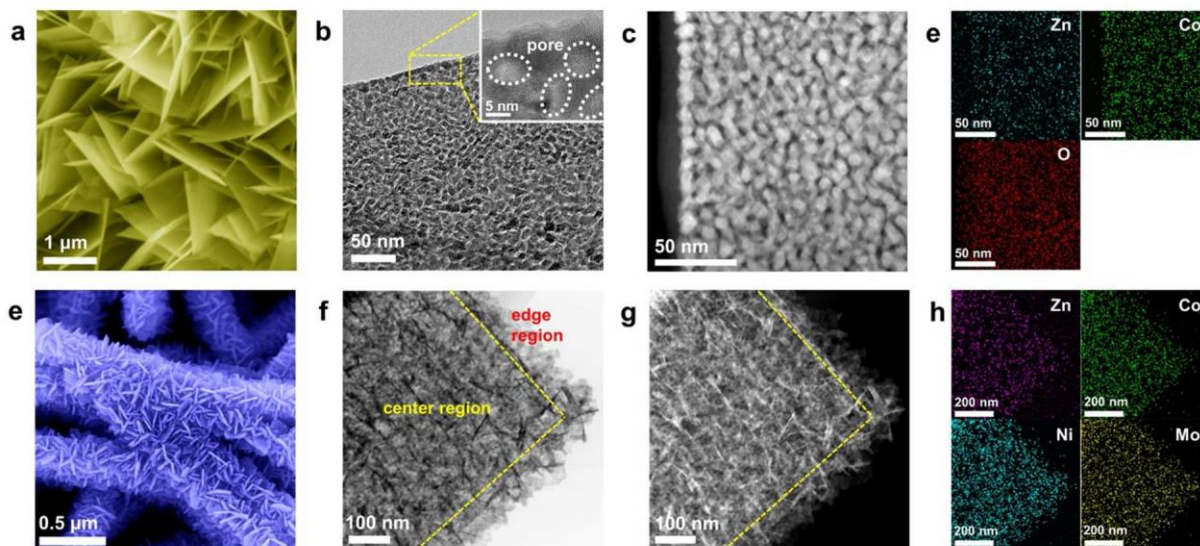


Figure 2. (a) SEM, (b) TEM, (c) HADDF-STEM, and (d) EDX mapping images of 3D nanoporous  $\text{ZnCo}_2\text{O}_4$  serving as a back-bone structure. The inset image in Figure 2b indicates highly porous grains of  $\text{ZnCo}_2\text{O}_4$ . (e) SEM, (f) STEM, (g) HADDF-STEM, and (h) EDX mapping images of hierarchically assembled 3D  $\text{ZnCo}_2\text{O}_4/\text{NiMoO}_4$  heterostructures.

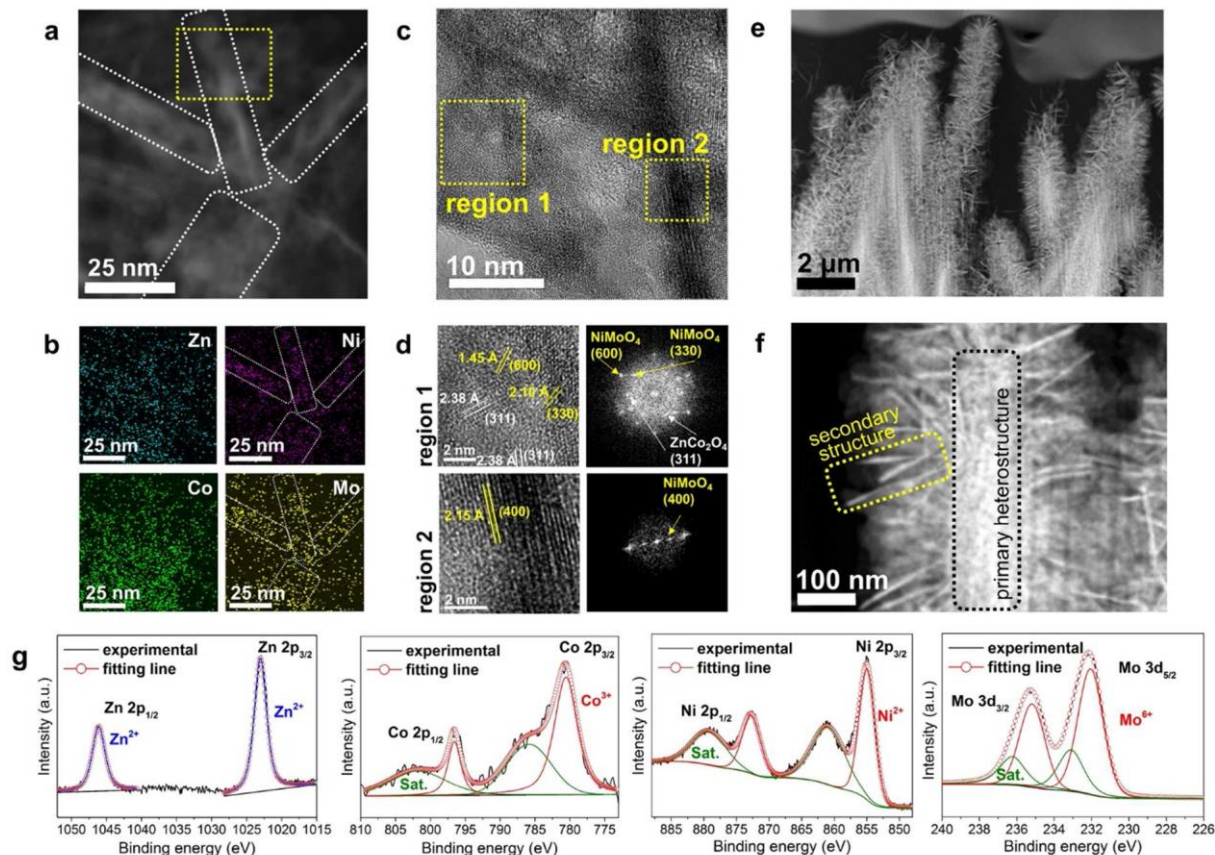


Figure 3. (a) A high-resolution HAADF-STEM and (b) EDX elemental mapping images of  $\text{ZnCo}_2\text{O}_4/\text{NiMoO}_4$  heterostructures. (c) A high-resolution TEM image of  $\text{ZnCo}_2\text{O}_4/\text{NiMoO}_4$  heterostructures taken from the region outlined by the yellow dotted rectangle in Figure 3a. (d) High-resolution TEM and FFT images of the region 1 indicate existence of primary heterostructures of the  $\text{NiMoO}_4$  shell and the rigid  $\text{ZnCo}_2\text{O}_4$  core. High-resolution TEM and FFT images of region 2 indicate existence of secondary layered  $\text{NiMoO}_4$  nanosheets. (e) A low-resolution and (f) high-resolution cross sectional HAADF-STEM images of  $\text{ZnCo}_2\text{O}_4/\text{NiMoO}_4$  heterostructures. (g) XPS Zn 2p, Co 2p, Ni 2p, and Mo 3d spectra of  $\text{ZnCo}_2\text{O}_4/\text{NiMoO}_4$  heterostructures.

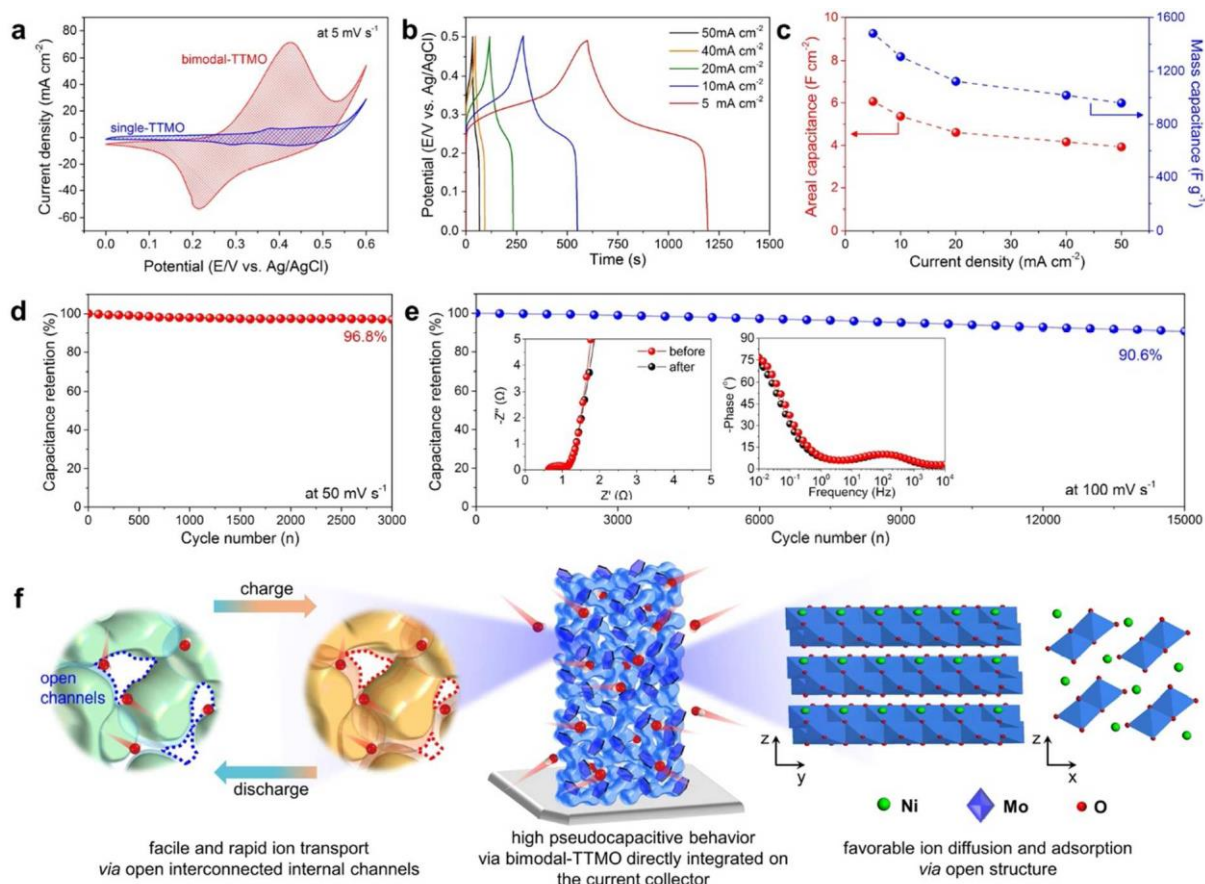


Figure 4. (a) CV curves of bimodal-TTMO and single-TTMO at a scan rate of  $5 \text{ mV s}^{-1}$ . (b) GCD curves of bimodal-TTMO at different current densities. (c) Specific capacitances of bimodal-TTMO at different current densities. (d) Cycle performance of bimodal-TTMO at a scan rate of  $50 \text{ mV s}^{-1}$  up to 3000 cycling charge/discharge tests. (e) Under harsh conditions, cycle performance of bimodal-TTMO at a scan rate of  $100 \text{ mV s}^{-1}$  up to 15000 cycling charge/discharge tests. The insets in Figure 4e indicate Nyquist plots and Bode plots of bimodal-TTMO before and after long-term cycling tests. (f) Illustration showing pseudo-capacitive behavior in hierarchically assembled 3D  $\text{ZnCo}_2\text{O}_4/\text{NiMoO}_4$  heterostructures.

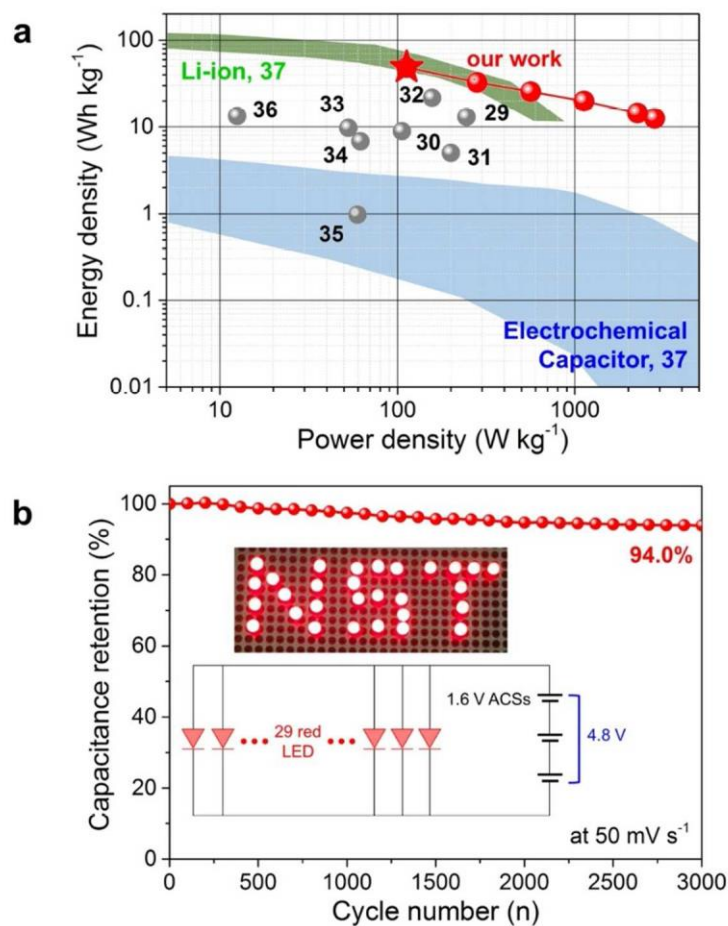


Figure 5. (a) Ragone plots of the AC//ZnCo<sub>2</sub>O<sub>4</sub>/NiMoO<sub>4</sub> ASC as well as other, recently reported, pseudo-capacitive ASCs. (b) Cycle performance of the AC//ZnCo<sub>2</sub>O<sub>4</sub>/NiMoO<sub>4</sub> ASC at a scan rate of  $50 \text{ mV s}^{-1}$  up to 3000 cycling charge/discharge tests. The inset in Figure 5b are photographs showing three ASCs in series that can light up 29 red LEDs.

1  
2  
3 **ASSOCIATED CONTENT**

4  
5  
6 **Supporting Information.** Additional structural and electrochemical analysis data in Figure S1-  
7  
8  
9 S10 and Table S1.

13  
14 **AUTHOR INFORMATION**

15  
16  
17 **Corresponding Author**

18  
19  
20 \*E-mail: shin@unist.ac.kr (H.S.S.) and junginn.sohn@eng.ox.ac.uk (J.I.S.)  
21

22  
23 **Author Contributions**

24  
25  
26 ‡These authors contributed equally.  
27

28  
29 **Notes**

30  
31 The authors declare no competing financial interest.  
32

33  
34 **ACKNOWLEDGMENT**

35  
36 This research was supported by the Industrial Fundamental Technology Development Program  
37  
38 (10052745, Development of the nano-sized (100 nm) manganese ceramic material for high  
39  
40  
41  
42 voltage pseudo-capacitor) funded by the Ministry of Trade, Industry and Energy (MOTIE) of  
43  
44 Korea, and the European Research Council under the European Union's Seventh Framework  
45  
46 Programme (FP/2007-2013)/Grant Agreement no. 685758, Project '1D-NEON'. In addition,  
47  
48  
49 SMM would also like to thank The Royal Society for financial support.

## REFERENCES

- (1) Dresselhaus, M. S.; Thomas, I. L. Alternative Energy Technologies. *Nature* **2001**, *414*, 332–337.
- (2) Miller, J.; Simon, P. Electrochemical Capacitors for Energy Management. *Science* **2008**, *321*, 651–652.
- (3) Salanne, M.; Rotenberg, B.; Naoi, K.; Kaneko, K.; Taberna, P.-L.; Grey, C. P.; Dunn, B.; Simon, P. Efficient Storage Mechanisms for Building Better Supercapacitors. *Nat. Energy* **2016**, *1*, 16070.
- (4) Peng, Y.-Y.; Akuzum, B.; Kurra, N.; Zhao, M.-Q.; Alhabeib, M.; Anasori, B.; Kumbur, E. C.; Alshareef, H.; Ger, M.-D.; Gogotsi, Y. All-MXene (2D Titanium Carbide) Solid-State Microsupercapacitors for On-Chip Energy Storage. *Energy Environ. Sci.* **2016**, *9*, 2847–2854.
- (5) Simon, P.; Gogotsi, Y.; Dunn, B. Where Do Batteries End and Supercapacitors Begin?. *Science* **2014**, *343*, 1210–1211.
- (6) Arico, A. S.; Bruce, P.; Scrosati, B.; Tarascon, J.-M.; Schalkwijk, W. Nanostructured Materials for Advanced Energy Conversion and Storage Devices. *Nat. Mater.* **2005**, *4*, 366–377.
- (7) Wang, G.; Zhang, L.; Zhang, J. A Review of Electrode Materials for Electrochemical Supercapacitors. *Chem. Soc. Rev.* **2012**, *41*, 797–828.
- (8) Li, X.; Jiang, L.; Zhou, C.; Liu, J.; Zeng, H. Integrating Large Specific Surface Area and High Conductivity in Hydrogenated NiCo<sub>2</sub>O<sub>4</sub> Double-Shell Hollow Spheres to Improve Supercapacitors. *NPG Asia Mater.* **2015**, *7*, e165.

- 1  
2  
3  
4  
5  
6  
7  
8  
9  
10  
11  
12  
13  
14  
15  
16  
17  
18  
19  
20  
21  
22  
23  
24  
25  
26  
27  
28  
29  
30  
31  
32  
33  
34  
35  
36  
37  
38  
39  
40  
41  
42  
43  
44  
45  
46  
47  
48  
49  
50  
51  
52  
53  
54  
55  
56  
57  
58  
59  
60
- (9) Chen, H.; Hu, L.; Chen, M.; Yan, Y.; Wu, L. Nickel–Cobalt Layered Double Hydroxide Nanosheets for High-performance Supercapacitor Electrode Materials. *Adv. Funct. Mater.* **2014**, *24*, 934–942.
- (10) Toupin, M.; Brousse, T.; Bélanger, D. Charge Storage Mechanism of MnO<sub>2</sub> Electrode Used in Aqueous Electrochemical Capacitor. *Chem. Mater.* **2004**, *16*, 3184–3190.
- (11) Lee, Y.-W.; Kim, B.-S.; Hong, J.; Lee, J.; Pak, S.; Jang, H.-S.; Whang, D.; Cha, S.-N.; Sohn, J. I.; Kim, J. M. A Pseudo-Capacitive Chalcogenide-Based Electrode with Dense 1-Dimensional Nanoarrays for Enhanced Energy Density in Asymmetric Supercapacitors. *J. Mater. Chem. A* **2016**, *4*, 10084–10090.
- (12) Mefford, T.; Hardin, W.; Dai, S.; Johnston, K.; Stevenson, K. Anion Charge Storage through Oxygen Intercalation in LaMnO<sub>3</sub> Perovskite Pseudocapacitor Electrodes. *Nat. Mater.* **2014**, *13*, 726–732.
- (13) Chen, D.; Wang, Q.; Wang, R.; Shen, G. Ternary Oxide Nanostructured Materials for Supercapacitors: A Review. *J. Mater. Chem. A* **2015**, *3*, 10158–10173.
- (14) Ren, X.; Guo, C.; Xu, L.; Li, T.; Hou, L.; Wei, Y. Facile Synthesis of Hierarchical Mesoporous Honeycomb-like NiO for Aqueous Asymmetric Supercapacitors. *ACS Appl. Mater. Interfaces* **2015**, *7*, 19930–19940.
- (15) Qiu, Y.; Yang, S.; Deng, H.; Jin, L.; Li, W. A Novel Nanostructured Spinel ZnCo<sub>2</sub>O<sub>4</sub> Electrode Material: Morphology Conserved Transformation from a Hexagonal Shaped Nanodisk Precursor and Application in Lithium Ion Batteries. *J. Mater. Chem.* **2010**, *20*, 4439–4444.
- (16) Liu, B.; Zhang, J.; Wang, X.; Chen, G.; Chen, D.; Zhou, C.; Shen, G. Hierarchical Three-Dimensional ZnCo<sub>2</sub>O<sub>4</sub> Nanowire Arrays/Carbon Cloth Anodes for a Novel



- 1  
2  
3 Class of High-Performance Flexible Lithium-Ion Batteries. *Nano Lett.* **2012**, *12*, 3005–  
4  
5 3011.  
6  
7  
8 (17) Zhang, D.; Zhang, Y.; Li, X.; Luo, Y.; Huang, H.; Wang, J.; Chu, P. K. Self-Assembly  
9  
10 of Mesoporous ZnCo<sub>2</sub>O<sub>4</sub> Nanomaterials: Density Functional Theory Calculation and  
11  
12 Flexible All-Solid-State Energy Storage. *J. Mater. Chem. A* **2016**, *4*, 568–577.  
13  
14  
15 (18) Yin, Z.; Zhang, S.; Chen, Y.; Gao, P.; Zhu, C.; Yang, P.; Qi, L. Hierarchical  
16  
17 Nanosheet-Based NiMoO<sub>4</sub> Nanotubes: Synthesis and High Supercapacitor  
18  
19 Performance. *J. Mater. Chem. A* **2015**, *3*, 739–745.  
20  
21  
22 (19) Xiao, K.; Xia, L.; Liu, G.; Wang, S.; Ding, L.-X.; Wang, H. Honeycomb-like NiMoO<sub>4</sub>  
23  
24 Ultrathin Nanosheet Arrays for High-Performance Electrochemical Energy Storage. *J.*  
25  
26 *Mater. Chem. A* **2015**, *3*, 6128–6135.  
27  
28  
29 (20) Gai, Y.; Shang, Y.; Gong, L.; Su, L.; Hao, L.; Dong, F.; Li, J. A Self-Template  
30  
31 Synthesis of Porous ZnCo<sub>2</sub>O<sub>4</sub> Microspheres for High-Performance Quasi-Solid-State  
32  
33 Asymmetric Supercapacitors. *RSC Adv.* **2017**, *7*, 1038–1044.  
34  
35  
36 (21) Peng, S.; Li, L.; Wu, H. B.; Madhavi, S.; Lou, X. W. Controlled Growth of NiMoO<sub>4</sub>  
37  
38 Nanosheet and Nanorod Arrays on Various Conductive Substrates as Advanced  
39  
40 Electrodes for Asymmetric Supercapacitors. *Adv. Energy Mater.* **2015**, *5*, 1401172.  
41  
42  
43 (22) Gao, G.; Wu, H. B.; Dong, B.; Ding, S.; Lou, X. W. Growth of Ultrathin ZnCo<sub>2</sub>O<sub>4</sub>  
44  
45 Nanosheets on Reduced Graphene Oxide with Enhanced Lithium Storage Properties.  
46  
47 *Adv. Sci.* **2015**, *2*, 1400014.  
48  
49  
50 (23) Huang, L.; Zhang, W.; Xiang, J.; Xu, H.; Li, G.; Huang, Y. Hierarchical Core-Shell  
51  
52 NiCo<sub>2</sub>O<sub>4</sub>@NiMoO<sub>4</sub> Nanowires Grown on Carbon Cloth as Integrated Electrode for  
53  
54 High-Performance Supercapacitors. *Sci. Rep.* **2016**, *6*, 31465.  
55  
56  
57  
58  
59  
60

- 1  
2  
3 (24) Qiu, K.; Lu, Y.; Zhang, D.; Cheng, J.; Yan, H.; Xu, J.; Liu, X.; Kim, J.-K.; Luo, Y.  
4  
5  
6 Mesoporous, hierarchical core/shell structured ZnCo<sub>2</sub>O<sub>4</sub>/MnO<sub>2</sub> nanocone forests for  
7  
8 high-performance supercapacitors. *Nano Energy* **2015**, *11*, 687–696.  
9  
10 (25) Hong, J.; Lee, Y.-W.; Hou, B.; Ko, W.; Lee, J.; Pak, S.; Hong, J.-P.; Morris, S.; Cha,  
11  
12 S.-N.; Sohn, J. I.; Kim, J. M. Solubility-Dependent NiMoO<sub>4</sub> Nanoarchitectures: Direct  
13  
14 Correlation between Rationally Designed Structure and Electrochemical  
15  
16 Pseudokinetics. *ACS Appl. Mater. Interfaces* **2016**, *8*, 35227–35234.  
17  
18 (26) Wang, H.; Yi, H.; Zhu, C.; Wang, X.; Fan, H. J. Functionalized Highly Porous  
19  
20  
21 Graphitic Carbon Fibers for High-Rate Supercapacitive Electrodes. *Nano Energy*  
22  
23 **2015**, *13*, 658–669.  
24  
25 (27) Yuan, L.; Lu, X.-H.; Xiao, X.; Zhai, T.; Dai, J.; Zhang, F.; Hu, B.; Wang, X.; Gong,  
26  
27 L.; Chen, J.; Hu, C.; Tong, Y.; Zhou, J.; Wang, Z. L. Flexible Solid-State  
28  
29 Supercapacitors Based on Carbon Nanoparticles/MnO<sub>2</sub> Nanorods Hybrid Structure.  
30  
31 *ACS Nano* **2012**, *6*, 656–661.  
32  
33 (28) Masikhwa, T.; Madito, M.; Momodu, D.; Dangbegnon, J.; Guellati, O.; Harat, A.;  
34  
35  
36 Guerioune, M.; Barzegar, F.; Manyala, N. High Performance Asymmetric  
37  
38 Supercapacitor Based on CoAl-LDH/GF and Activated Carbon from Expanded  
39  
40 Graphite. *RSC Adv.* **2016**, *6*, 46723–46732.  
41  
42  
43 (29) Cai, D.; Wang, D.; Liu, B.; Wang, Y.; Liu, Y.; Wang, L.; Li, H.; Huang, H.; Li, Q.;  
44  
45  
46 Wang, T. Comparison of the Electrochemical Performance of NiMoO<sub>4</sub> Nanorods and  
47  
48 Hierarchical Nanospheres for Supercapacitor Applications. *ACS Appl. Mater.*  
49  
50 *Interfaces* **2013**, *5*, 12905–12910.  
51

- 1  
2  
3 (30) Cheng, Y.; Lu, S.; Zhang, H.; Varanasi, C.; Liu, J. Synergistic Effects from Graphene  
4 and Carbon Nanotubes Enable Flexible and Robust Electrodes for High-Performance  
5 Supercapacitors. *Nano Lett.* **2012**, *12*, 4206–4211.  
6  
7  
8  
9  
10 (31) Cai, W.; Lai, T.; Dai, W.; Ye, J. A Facile Approach to Fabricate Flexible All-Solid-  
11 State Supercapacitors Based on  $\text{MnFe}_2\text{O}_4$ /Graphene Hybrids. *J. Power Sources* **2014**,  
12 *255*, 170–178.  
13  
14  
15 (32) Cheng, D.; Yang, Y.; Xie, J.; Fang, C.; Zhang, G.; Xiong, J. Hierarchical  
16  $\text{NiCo}_2\text{O}_4$ @ $\text{NiMoO}_4$  Core-Shell Hybrid Nanowire/Nanosheet Arrays for High-  
17 Performance Pseudocapacitors. *J. Mater. Chem. A* **2015**, *3*, 14348–14357.  
18  
19  
20 (33) Zou, B.-X.; Liang, Y.; Liu, X.-X.; Diamond, D.; Lau, K.-T. Electrodeposition and  
21 Pseudocapacitive Properties of Tungsten Oxide/Polyaniline Composite. *J. Power*  
22 *Sources* **2011**, *196*, 4842–4848.  
23  
24  
25 (34) He, Y.; Chen, W.; Li, X.; Zhang, Z.; Fu, J.; Zhao, C.; Xie, E. Freestanding Three-  
26 Dimensional Graphene/ $\text{MnO}_2$  Composite Networks as Ultralight and Flexible  
27 Supercapacitor Electrodes. *ACS Nano* **2013**, *7*, 174–182.  
28  
29  
30  
31 (35) Ramasamy, K.; Gupta, R.; Palchoudhury, S.; Ivanov, S.; Gupta, A. Layer-Structured  
32 Copper Antimony Chalcogenides ( $\text{CuSbSe}_x\text{S}_{2-x}$ ): Stable Electrode Materials for  
33 Supercapacitors. *Chem. Mater.* **2015**, *27*, 379–386.  
34  
35  
36  
37 (36) Foo, C. Y.; Sumboja, A.; Tan, D. J. H.; Wang, J.; Lee, P. S. Flexible and Highly  
38 Scalable  $\text{V}_2\text{O}_5$ -rGO Electrodes in an Organic Electrolyte for Supercapacitor Devices.  
39 *Adv. Energy Mater.* **2014**, *4*, 1400236.  
40  
41  
42  
43 (37) Simon, P.; Gogotsi, Y. Materials for Electrochemical Capacitors. *Nat. Mater.* **2008**, *7*,  
44 845–854.  
45  
46  
47  
48  
49  
50  
51  
52  
53  
54  
55  
56  
57  
58  
59  
60

1  
2  
3 **Table of Contents**  
4  
5  
6  
7  
8  
9  
10  
11  
12  
13  
14  
15  
16  
17  
18  
19  
20  
21  
22  
23  
24  
25  
26  
27  
28  
29  
30  
31  
32  
33  
34  
35  
36  
37  
38  
39  
40  
41  
42  
43  
44  
45  
46  
47  
48  
49  
50  
51

